PIV study of fractal grid turbulence

S. Discetti[1], I. B. Ziskin[2], R. J. Adrian[2], K. Prestridge[3]

[1]Dipartimento di Ingegneria Aerospaziale (DIAS), University of Naples Federico II, Naples, Italy
stefano.discetti@unina.it

[2]School for Engineering of Matter, Transport and Energy, Arizona State University,
Tempe, AZ, 85287-6106, USA

[3]Los Alamos National Laboratory, Los Alamos NM 8754, USA

ABSTRACT

The present work describes an experimental investigation of the decay of the wind tunnel turbulence generated by space filling fractal square grids by means of stereoscopic Particle Image Velocimetry (PIV). PIV is severely challenged by measurements of power spectra and measurements of low turbulence intensity flow, and this application involves both. Good statistics require averages over large numbers of frames, and the authors discuss the statistical convergence. Among the quantities to be analysed from the obtained velocity fields are the longitudinal integral length scale, Taylor micro-scale, streamwise two-point correlation functions, and energy spectra.

1. INTRODUCTION

Multi-scale generated turbulence has unusual properties that may lead to exciting new insights into turbulence theory as well as important new industrial applications. The study of turbulence generated by fractal elements is motivated by the *dissipation anomaly* (i.e. the independence of the turbulent kinetic dissipation rate on Reynolds number at high Re), which lies at the root of Kolmogorov's theory. When turbulence is generated by injecting energy over a range of length scales, as by a fractal grid, the spectral energy transfer mechanism can be investigated by adjusting the geometry of the fractal grid [1].

Hurst and Vassilicos [2] found that space-filling fractal square grids gave the most interesting results, showing an increase of the turbulence intensity until a downstream location x_{peak}, and a subsequent exponential decay, as opposed to the well-known power law decay of classical square grids [3-4]. During the exponential decay, they found that the ratio of the longitudinal integral length scale L_{11} to the Taylor microscale λ is nearly constant. Furthermore, Seoud and Vassilicos [5] observed that fractal square grids can generate turbulence of about three times higher Reynolds number Re_λ than turbulence generated by classical grids, and comparable to turbulence generated by jet grids [6] and active grids [7] with the same flow speed and significantly lower blockage ratio.

All measurements to date have been made using the hot-wire anemometer. The measurement of power spectra and turbulence statistics is, in low turbulence intensity flow, a challenge for PIV. However, up-to-date cameras allow high spatial resolution, enabling the possibility to extract turbulence statistics from the flow field. In the present work we present a Stereo PIV investigation of fractal/multiscale-generated turbulence. In Sec. 2 the geometry of the adopted space-filling fractal grids is presented; in Sec. 3 the experimental setup, and the test procedure are described. In Sec. 4 the statistical convergence is discussed and the results are shown.

2. SPACE-FILLING FRACTAL GRIDS

The fractal grids consist of the repetition of a specific pattern at different scales (see figure 1). In the present work we use a square pattern, which consists of four bars. The length and the thickness of each bar at the j-th iteration are indicated with the symbols L_j and t_j, respectively. The grids are space filling, i.e. their fractal dimension D_f is equal to 2 (the definition of D_f can be found in [2]). At the j-th iteration there are four times more patterns of the *(j-1)-th* iteration, while the length and the thickness are reduced by the scaling factors R_L and R_t.
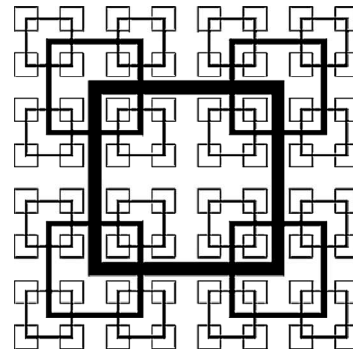

Figure 1. Example of space-filling multiscale/fractal grid with square generating pattern.

Three fractal grids have been used, with different thickness ratios (i.e. the ratio between of the largest to the smallest bar thicknesses) t_r (8.5, 13 and 17, respectively) and only slightly different average blockage ratio σ and effective mesh-length M_{eff}, calculated as in [2]. The complete details about the geometry of the grids are reported in Table 1.

tr	RL	Rt	σ	Meff [mm]
8.5	0.5	0.490	0.25	15.78
13	0.5	0.425	0.32	15.17
17	0.5	0.389	0.37	14.62

Table 1. Fractal grid parameters

3. EXPERIMENTAL SETUP

The grids are tested in a low turbulence level open circuit wind tunnel, with a $L=1,524mm$ long and $T=152.4mm$ wide square test section. The fractal grid is placed at the inlet of the test section, immediately after the contraction. The residual

level of turbulence in absence of the grid is lower than 0.5% along the centerline of the wind tunnel. The test Reynolds number, based on the velocity at the exit section of the contraction without the grids, and the effective mesh-length of the fractal grid, ranges between 8,500 and 9,200 (depending on the fractal grid).

Seeding, in the form of oil droplets of diameter of approximately 1µm, is injected uniformly into the fluid flow. It is illuminated by a laser light sheet, generated by double-cavity Nd-YAG laser, with a thickness of about 0.5mm, a pulse duration of 8ns, a pulse frequency of 2Hz and a maximum energy per pulse of 100mJ.

The experiments are carried out with an angular, symmetric stereoscopic PIV configuration, with cameras placed at +40°, -40°. TSI POWERVIEW™ Plus 11MP cameras (4008 x 2672 pixels), equipped with Nikon objectives with a focal length of 60mm, are employed to record images with about 22 pixels/mm resolution. The Scheimpflug condition [8] is satisfied to obtain uniform focusing of the images.

A grid of dots, with diameter of 0.5mm and spacing of 5mm, has been generated to perform the optical calibration of the system. A translation stage moves the calibration target along the z direction (where the x and y axis coincide with the streamwise and crosswise directions in the light sheet plane, and the z axis completes the three dimensional orthogonal reference system pointing towards the cameras) with an accuracy of 13μm. Polynomial mapping functions of the third order in x, y, and z, are employed to fit the correspondence between world and image coordinates. The misalignment correction between the laser sheet and the z=0 plane is performed as proposed by Wieneke [9]. The so called disparity map is computed on 50 samples, and then averaged to suppress the effect of noise.

The imaging system is placed in three streamwise locations, in order to investigate the characteristics of the evolution of the generated structures throughout their decay history, and to assess the sensitivity of the measurement setup in detecting the level of turbulence intensity. The two-component displacement fields are obtained by interrogating the two warped images with a standard homebuilt multi-pass PIV software with window deformation, as described in [10], and the three-component (3C) displacement field is computed by a procedure including both dewarping and 3C reconstruction, as proposed by Soloff et al. [11]. The final dimension of the interrogation spot is 16 x 16 $pixels$ = 0.727 x 0.727 mm with 50% overlap. The results are averaged over 500 realizations.

4. RESULTS

4.1 Instantaneous velocity fields

In this section some features of the instantaneous velocity field are briefly illustrated. The flow is characterized by a range of length scales and structures. In figure 2 (top) an example of instantaneous distribution of the z-component of the vorticity is illustrated. The flow field is smoothed by a Gaussian filtering window, with a 3 x 3 kernel and a standard deviation equal to 1.

A magnified illustration of the highlighted zone is presented in figure 2, bottom. The vector representation of the fluctuating velocity field is also reported. The turbulent structures composed of scales of the order of the Taylor micro-scale of the motion are satisfactorily resolved. The Taylor micro-scale, calculated as described in Sec. 4.4, is of approximately 2.6mm, i.e. about 3.7 times the linear dimension of the interrogation spot.
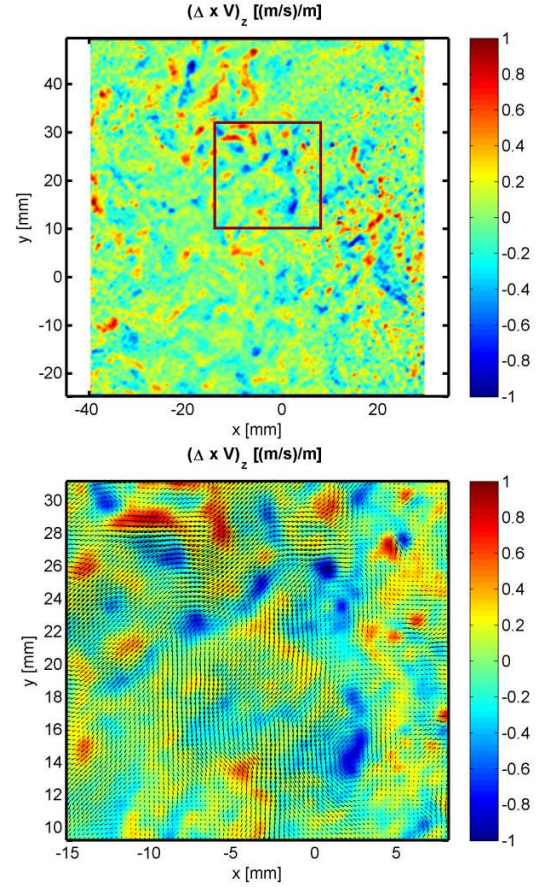

Figure 2. Top: Instantaneous z-vorticity field, for the fractal grid with t_r=8.5 at the first streamwise location. Bottom: magnified version of the highlighted zone in figure 2, top, and vector representation of the fluctuating velocity field.
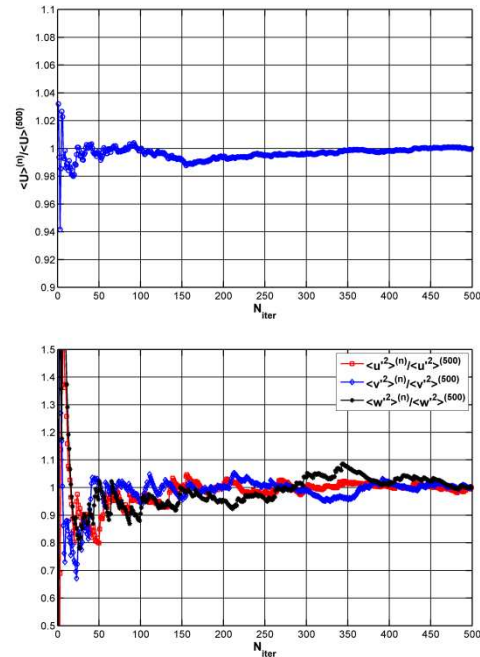

Figure 3. History of statistical convergence of the averaged streamwise velocity (top) and of the averaged square fluctuations (bottom).

4.2 Statistical convergence

Reliable evaluation of the turbulence statistics requires averaging over a sufficient number of frames. In this section, we discuss the statistical convergence of the results, considering the experiment with the fractal grid having t_r=8.5 at the first tested streamwise location. The history of convergence is reported in figure 3 for the mean velocity and the mean squared fluctuations at the location in the centre of the image. The results are normalized by $<f>^{(500)}$, the corresponding value averaged over the total number of realizations, where $<f>^{(n)}$ is the value of the generic physical quantity f averaged over n independent realizations.

The results show fast convergence of the streamwise velocity (the average value changes of less than 1% after 200 realizations), while the noise effect is much stronger on the mean squared fluctuation (more than 400 samples are needed to reduce the variation below 3%).

4.3 Mean flow features

In this section the extracted mean flow features are presented. The average streamwise velocity component (see figure 4) has a jet-like distribution, confirming the results of [2]. This is due to the relative low blockage ratio close to the centreline of the wind tunnel. Moving downstream, the homogeneity of the velocity distribution improves.

Regarding the squared fluctuations, the decay along the tunnel centreline is clearly detectable in fig. 5-6; this results was expected, since the streamwise coordinate of the peak of turbulence intensity x_{peak}=0.5·x^*=0.5·L_0^2/t_0 is equal to approximately 29.1, 26.2 and 23.8 mesh lengths for the three fractal grid with thickness ratio equal to 8.5, 13 and 17, respectively.

The Stereo PIV technique seems to be able to identify the anisotropy of the turbulent fluctuations, as expected [2]. On the other hand, the effect of noise makes it difficult to fit the decay to understand whether it is exponential or not. Furthermore, the fluctuation of the out-of-plane velocity component is consistently higher than that of the crosswise velocity component. This effect is due to sensitivity of the stereoscopic reconstruction algorithm in evaluating the out-of-plane displacement, since, for symmetry arguments, the true mean square out-of-plane velocity fluctuation should be more nearly equal to the mean square cross-stream velocity fluctuation.
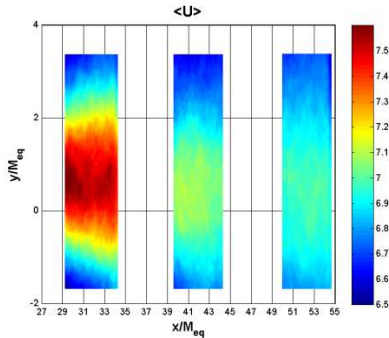

Figure 4. Average streamwise velocity field for the grid t_r=8.5, in *m/s.*

4.4 Turbulent statistics

The measured velocity fields are analysed to extract information about the turbulence statistics. Among the others, the normalized longitudinal two-point correlation function of the fluctuating velocity component $u(x)$ (see figure 7) is calculated as follows:

$$f(x,r) = \frac{\langle u(x+r) \cdot u(x)\rangle}{\langle u^2(x)\rangle}$$

The longitudinal integral length scale L_u is obtained by taking the integral from zero to infinity of the normalized longitudinal two-point correlation function. The longitudinal Taylor micro-scale λ_f is calculated from the second derivative of f. One can also estimate the Kolmogorov length scale:

$$\eta = \left(\frac{\upsilon^2}{15\langle(\partial u/\partial x)^2\rangle}\right)$$

where υ is the kinematic viscosity of the fluid. The estimated average values of the aforementioned turbulent statistics are reported in Table 2 in the case of the fractal grid with t_r=8.5 at the most upstream location, with the aim of informing the reader as to the order of magnitude of the most relevant physical quantities.

L_{11}	λ_f	η
13-14*mm*	2-3*mm*	0.1-0.2*mm*

Table 2. Main flow features for the fractal grid with *tr*=8.5 at the most upstream location.
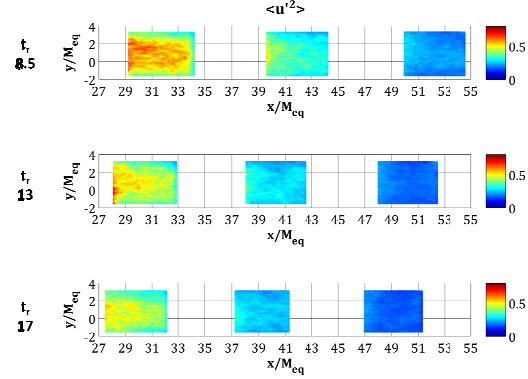

Figure 5. Average streamwise squared fluctuations (m^2/s^2) for 3 thickness ratios and streamwise locations.
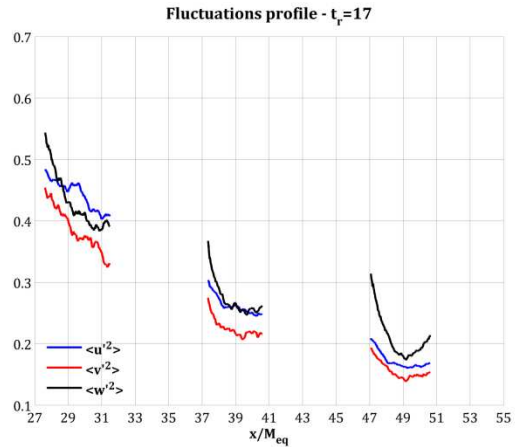

Figure 6. Velocity squared fluctuations profile, for t_r=17, in $m^2/s^2.$
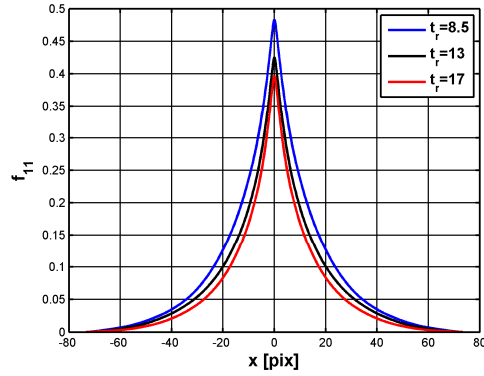
Figure 7. Longitudinal auto-correlation function for three thickness ratios at the first streamwise location.

The energy spectrum at the three tested streamwise locations for the fractal grid with t_r=8.5 are reported in figure 8. As observed by Seoud and Vassilicos [5], quite surprisingly, even in absence of the dissipation anomaly, the 1D longitudinal energy spectrum is proportional to $k^{-5/3}$, where k is the wave number, in the decay region, i.e. beyond the peak of turbulence intensity. The increase of the magnitude of the energy spectra at high wavenumbers are due to the significance of random measurement error at these smallest resolved displacements.
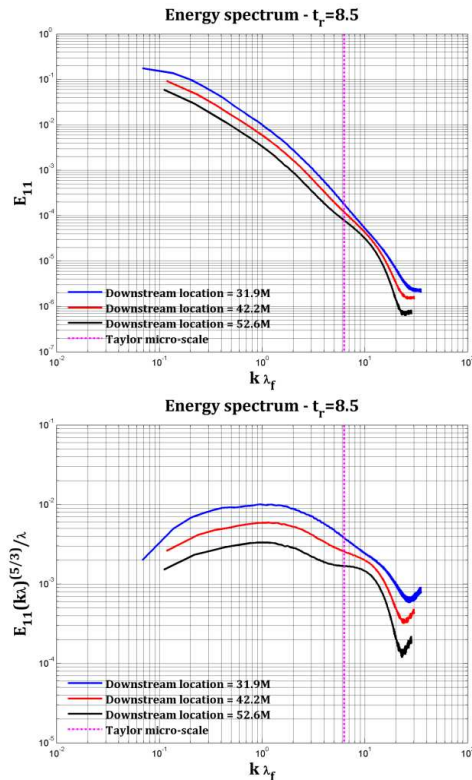

Figure 8. 1D energy spectra (compensated, in the lower figure), fractal grid with t_r=8.5, for three streamwise location.

5. CONCLUSIONS

A Stereo-PIV study of the decay of multi-scale/fractal generated turbulence has been presented. This kind of investigation, involving calculation of turbulence statistics, such as energy spectra and average squared turbulent fluctuations, at the state of art is particularly challenging for PIV. In the present paper a preliminary performance assessment highlights that Stereo-PIV is capable of detecting the decay of the streamwise and crosswise velocity fluctuations in the light sheet plane, and the anisotropy of the flow field, while the out-of-plane fluctuation is affected by the reconstruction noise. Unfortunately, the detected decay of the in-plane velocity fluctuations is also strongly affected by noise, therefore a fitting to confirm the exponential decay observed by Hurst and Vassilicos [2] is not trivial to be performed.

Energy spectra are also presented, showing that the larger scales of the flow field are well resolved, but the smallest resolvable scales are of the order of the Taylor micro-scale.

REFERENCES

[1] Mazellier N. & Vassilicos J.C. (2010) Turbulence without Richardson-Kolmogorov cascade. *Physics of Fluids*, **22(7)**, 075101.

[2] Hurst D. & Vassilicos J.C. (2007) Scalings and decay of fractal-generated turbulence. *Physics of Fluids*, **19(3)**, 035103.

[3] Batchelor G.K. & Townsend A.A. (1948) Decay of isotropic turbulence in the initial period. In *Proc. 3rd Australian Conference on Laser Diagnostics in Fluid Mechanics and Combustion*, The University of Queensland, Australia, 48-55, 2-3 December.

[4] Comte-Bellot G. & Corrsin S. (1966) The use of a contraction to improve the isotropy of grid-generated turbulence. *Journal of Fluid-Mechanics*, **25(4)**, 657-682.

[5] Seoud R.E. & Vassilicos J.C. (2007) Dissipation and decay of fractal-generated turbulence. *Physics of Fluids*, **19(10)**, 105108.

[6] Gad-El-Hak M. & Corrsin S. (1974) Measurements of the nearly isotropic turbulence behind a uniform jet grid. *Journal of Fluid-Mechanics*, **62(1)**, 115-143.

[7] Mydlarski L. & Warhaft Z. (1996) On the onset of high-Reynolds-number grid-generated wind tunnel turbulence. *Journal of Fluid-Mechanics*, **320**, 331-368.

[8] Prasad A.K. & Jensen K. (1995) Scheimpflug stereocamera for particle image velocimetry in liquid flows. *Applied Optics*, **34(30)**, 7092-7099.

[9] Wieneke B. (2005) Stereo-PIV using self-calibration on particle images. *Experiments in Fluids*, **39(2)**, 267-280.

[10] Giordano R. & Astarita T. (2009) Spatial resolution of the Stereo-PIV technique. *Experiments in Fluids*, **46(4)**, 643-658.

[11] Soloff S.M., Adrian R.J. & Liu Z.C.. (1997) Distortion compensation for generalized stereoscopic particle image velocimetry. *Measurement Science & Technology*, **8(12)**, 1441-1454.